



6 where  $z$  is the propagation distance,  $I_p$  and  $I_s$  are beam intensities of the pump and Stokes light,  
7 respectively, and  $g_R(\Omega)$  is the frequency dependent Raman gain coefficient arising from the imaginary  
8 component of a material's nonlinear susceptibility. While this equation describes the behavior of Raman  
9 scattering at a cross-sectionally localized point in space, in general, the overall Raman strength for  
10 arbitrary beam shapes is also proportional to an intensity overlap integral  $\eta$  over the transverse plane [2],  
11 given by:

$$12 \quad \eta = \int I_p(r, \phi) \cdot I_s(r, \phi) r dr d\phi \quad (2)$$

13 where  $r$  and  $\phi$  are radial and azimuthal coordinates. In addition, Raman gain is maximized for co-  
14 polarized light, hence in chiral media, a circularly polarized pump induces unequal amounts of Raman  
15 signal in the two opposite spins, yielding what is known as Raman optical activity [3]. Therefore, Raman  
16 Stokes scattering typically occurs for co-polarized light and its strength is proportional to an *intensity*  
17 overlap integral – i.e., it is impervious to the phase of either the pump or Stokes light. While Raman  
18 scattering dynamics for ultrashort pulses yield distinctive effects such as the soliton self-frequency shift  
19 and soliton self-mode conversion [4-6] where the effect also depends on the group velocity and group-  
20 velocity dispersion of light in the medium, the underlying rules – spectral response being governed by  
21  $g_R(\Omega)$ , effect being *insensitive* to light's phase, and being maximized for co-polarized light – remain the  
22 same.

23 This is in contrast to well-known parametric nonlinearities such as second harmonic generation,  
24 four-wave-mixing [1] (FWM), or coherent anti-Stokes Raman scattering [7] (which is a special case of FWM),  
25 where phases of individual beams matter, and hence phase matching among the interacting photons  
26 determines the emission spectra [Fig. 1(a)]. The fundamental distinction is between elastic and inelastic  
27 scattering, Raman being of the latter variety, because a participating optical phonon mediates both energy

28 and momentum conservation. Since the magnitude of momentum carried by lattice vibrations is orders of  
29 magnitude greater than that carried by photons, optical phonon wavevectors at almost any arbitrary  
30 orientations in relation to those of the incident and scattered photons are able to offer momentum  
31 conservation for the scattering process [Fig. 1(b)]. Hence the Raman scattering process automatically  
32 conserves momentum, and since momentum is intimately tied to the phase of a photon, Raman is typically  
33 known to be a self-phase-matched process. This imperviousness to phase is actually a key attribute for  
34 Raman Stokes scattering, since spectral shapes of absorption lines are not influenced by properties of the  
35 pump beam such as the angle of incidence of light, or the dispersive properties of matter being probed  
36 etc., hence yielding a highly reliable fingerprinting tool for spectroscopy [8]. But this also means that it is  
37 inevitably present in all systems and can be detrimental in applications such as quantum source generation  
38 [9] or power-scaling of fiber lasers [10], where it either acts as a noise source or reduces device efficiency.  
39 Thus, reported schemes for suppressing Raman scattering have involved ‘brute-force’ methods such as  
40 reducing beam intensity [11], inhibiting transmission at Stokes wavelengths [12] or cooling the material  
41 [13] to decrease the magnitude of  $g_R(\Omega)$ . Even so, none of these techniques can significantly alter the  
42 spectral shape  $g_R(\Omega)$ , defined solely by the material. Here, we show that light carrying orbital angular  
43 momentum (OAM) that experiences spin-orbit coupling, as readily occurring due to the confining potential  
44 of an optical fiber waveguide, can fundamentally alter Stokes Raman scattering by making it sensitive to  
45 the phases of the participating beams. This enables, for the first time to our knowledge, dispersive control  
46 of the strength as well as spectrum of Raman Stokes scattering simply by tailoring the topological charge  
47 of light.

48 Eigenmodes in a circularly symmetric waveguide such as an optical fiber [14] carry both orbital  
49 angular momentum, which is quantified by the topological charge  $L$ , and spin angular momentum  $\hat{\sigma}^\pm$   
50 (left/right-handed circular polarization). Spin-orbit interaction (SOI), originating from the light-matter

51 interaction at dielectric interfaces, splits the effective refractive index ( $\Delta n_{eff}$ ) between  $\hat{\sigma}^{\pm}$  states of same  
52  $L$ , inducing optical activity [15] (OA). The ring-core fiber we use in our experiments [Fig. 1(c)] amplifies this  
53 SOI, enabling stable propagation of each  $\{L, \hat{\sigma}^{\pm}\}$  state. In addition, since this splitting is geometrodynamical  
54 in nature, optically active superpositions of these states, such as linearly polarized OAM modes, are also  
55 stable during propagation [15]. As a result, the polarization orientation angle of linearly polarized light  
56 carrying OAM at the input of the fiber systematically rotates as it propagates, with the beat length  $Z_{beat} =$   
57  $\lambda/\Delta n_{eff}$ . Schematic plots of this polarization evolution are shown in Figs. 1(d) and 1(e), which also  
58 illustrate a key attribute of such OA due to the SOI effect – Figure 1(d) illustrates this rotation for two  
59 eigenmodes, and it is evident that  $Z_{beat}$  varies strongly with topological charge, since SOI is known to be  
60 strongly dependent on topological charge (varies as  $L^3$  in the ring-core fibers used in our experiments, see  
61 Supplement 1). In addition, waveguide dispersion makes  $Z_{beat}$  a strong function of wavelength too. Thus,  
62 a spatially complex but deterministic polarization rotation effect typically dependent primarily on the  
63 material (dispersive) properties of chiral media [16], is now dependent on light's topological charge itself  
64 [Fig. 1(f)]. Now, considering the Raman interaction, we can quantify the spatial frequency ( $k = 2\pi/Z_{beat}$ )  
65 difference of the linear polarization rotation between a pump and Stokes photon for arbitrary mode  
66 combinations as:

$$67 \quad \Delta k = k_p - k_s = 2\pi \left[ \frac{\Delta n_{eff}^{(p)}(\lambda_p)}{\lambda_p} - \frac{\Delta n_{eff}^{(s)}(\lambda_s)}{\lambda_s} \right] \quad (3)$$

68 where, again,  $p$  and  $s$  represent pump and Stokes modes, respectively. When  $\Delta k \neq 0$ , which is the  
69 case for the majority of modes, Stokes light polarization walks off from the pump, see Fig. 1(d) – at every  
70 position  $z$  past the input, the linear polarization orientation of pump (red) differs from that of Stokes light  
71 (green), leading to reduction in Raman scattering, since Raman gain maximizes for co-polarized light. In  
72 contrast, as Fig. 1(e) illustrates, polarization rotation rates, and hence  $Z_{beat}$ , are matched, and hence  $\Delta k =$

73 0, over narrow Stokes spectral ranges in the special case when Stokes light in the mode order  $L_s = L_p - 1$   
 74 [denoted by the horizontal dashed lines of Fig. 1(f)]. In such a case, while Raman scattering is expected to  
 75 occur over the entire spectral region depicted by the grey band [Fig. 1(f)], polarization evolutions are

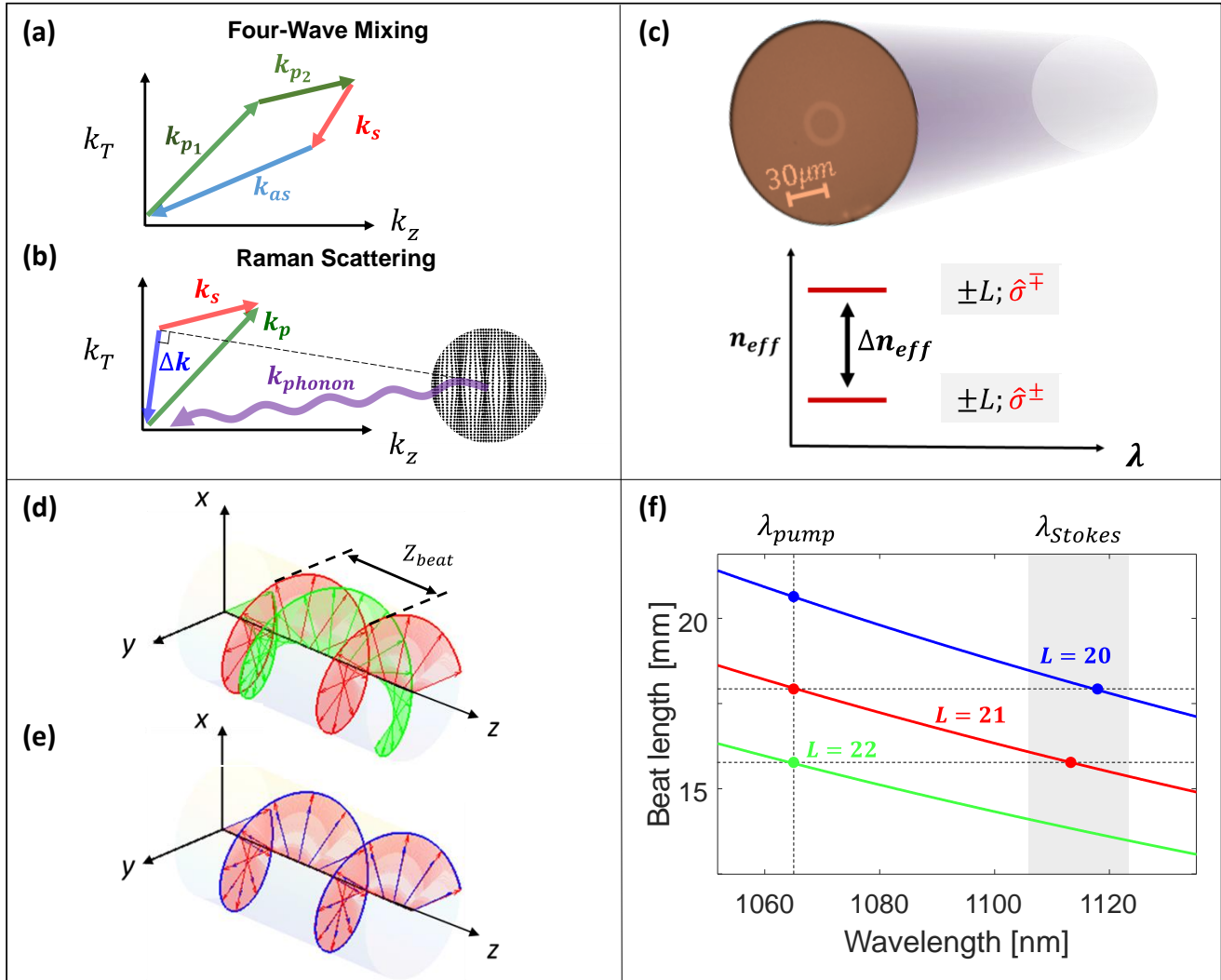


**Fig. 1. Phase-matched Stokes Raman scattering principle.** (a) Parametric nonlinear process such as four-wave-mixing requires momentum conservation of all interacting photons for maximum gain, arrows indicate wavevectors, and the subscript  $p_1$ ,  $p_2$ ,  $s$  and  $as$  represent two pumps, Stokes and anti-Stokes photons. (b) Stokes Raman scattering process is a phase-insensitive process as the optical phonons compensate for any phase mismatch between the pump and Stokes photons. (c) Facet image of the ring-core fiber used in the experiment, schematic plot of effective index splitting ( $\Delta n_{eff}$ ) between  $\hat{\sigma}^+$  and  $\hat{\sigma}^-$  of same  $L$  due to spin-orbit interaction. (d, e) Schematic plots of polarization evolution for optical activity modes of different topological charges at pump and Stokes wavelengths. Red: Pump light in  $L_p = 21$ , green: Stokes light in  $L_s = 22$ , blue: Stokes light in  $L_s = 20$ . (f) Beat length as a function of wavelength for different modes.

76 matched only at a specific wavelength within the grey Raman band, restricting Raman scattering to this  
77 region, where the  $\Delta k = 0$  condition is satisfied. Note that this is reminiscent of phase matching conditions  
78 for parametric nonlinear (as opposed to phonon-assisted Raman) processes, which maximizes only over  
79 the (relatively narrow) spectral range in which phase matching or momentum conservation is achieved,  
80 even if the underlying nonlinear susceptibility is broadband.

81

## 82 **Results:**

83 We probe this effect with a 650-ps, 1.7-kW-peak-power ( $P_{peak}$ ) pump source comprising a Nd:YAG  
84 laser and a fiber amplifier. This pump is converted to the desired OAM mode of a 9.8-m-long ring-core  
85 fiber [Fig. 1(c)] with a spatial light modulator (SLM), and another SLM is used to modally sort the output  
86 spectrum by the topological charge (see Supplement 1). We sweep  $L_p$  from 7 to 24 in both  $\hat{\sigma}^-$  and  $\hat{x}$  (OA)  
87 polarizations whose resultant measured mode intensity and phase profiles at the fiber output are shown  
88 in Fig. 2(b) (the details of the fiber and mode properties are discussed in Supplement 1). Similar ring shapes  
89 and sizes for all the modes result in similar nonlinear overlap integrals  $\eta$  [see Eq. (2)] for all different  
90 combinations of  $L_p$ 's and  $L_s$ 's – which is what conventionally controls the Raman scattering strength. To  
91 account for the slight differences, and hence to avoid any variations in Raman scattering strengths due to  
92 differing pump-Stokes overlaps, we adjust  $P_{peak}$  slightly for each  $L_p$  such that  $(P_{peak} \cdot \eta)$  remains  
93 constant throughout the experiments. For pumps in a pure circular polarization  $\hat{\sigma}^-$ , we observe that the  
94 Stokes light is also in  $\hat{\sigma}^-$ , and almost identical, conventionally co-polarized Raman spectra are obtained  
95 for all pump and Stokes mode combinations [17]. Given their similarity, for illustrative clarity, we only plot  
96 one of them ( $L_p = 7, \hat{\sigma}^-; L_s = 8, \hat{\sigma}^-$ ) as the red curves in Fig. 2(a). But when the pump is linearly polarized  
97 along  $\hat{x}$ , despite the fact that the spatial overlap,  $\eta$  still remains similar across all mode combinations, the

98 non-zero  $\Delta k$  terms for Stokes and pump combinations satisfying ( $L_S \neq L_p - 1$ ) result in complete  
 99 polarization walk-off between the pump and Stokes light [shown schematically in Fig. 1(d)], leading to  
 100 significant Raman gain reduction. Again, since all ( $L_S \neq L_p - 1$ ) yield similar spectra, Fig. 2(a) plots the

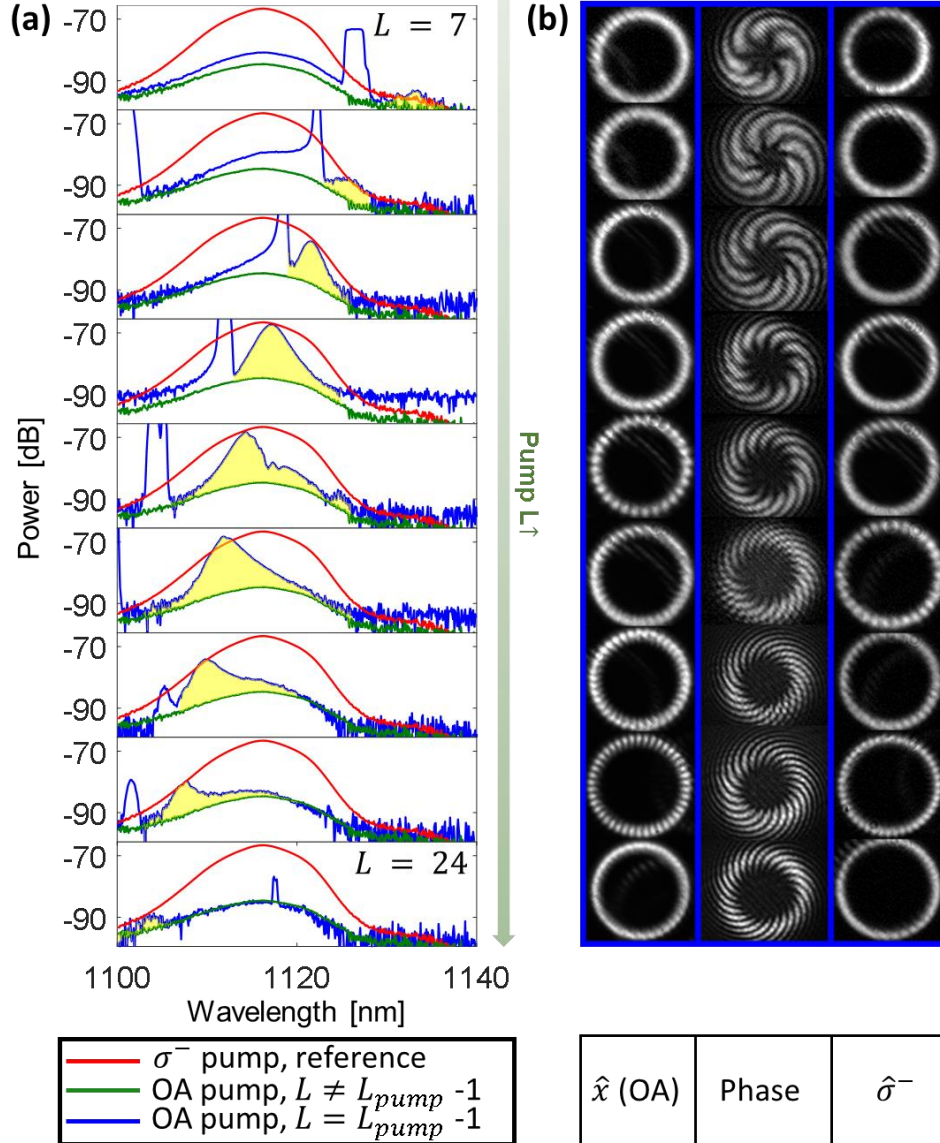


**Fig. 2. Raman spectra and pump mode images.** (a) Raman spectra plots for pump with different topological charges, arranged, top to bottom as  $L_p = 7, 8, 9, 11, 14, 17, 19, 21, 24$ ; Raman spectra shown as red curves represent {Stokes in  $L_S = 8$ ; Pump in  $L_p = 7, \hat{\sigma}^-$ } combinations; green curves represent  $\{L_S = 8; L_p = 7, \hat{x}\}$  combinations; and blue curves denote  $\{L_S = L_p - 1; L_p, \hat{x}\}$  combinations. The yellow shaded area represents contributions from the  $\Delta k = 0$  phase matching condition. (b) Left and right columns: Intensity distribution of pump modes in  $\hat{x}$  and  $\hat{\sigma}^-$  polarizations. Middle: Phase pattern acquire by interference with an expanded Gaussian beam, the number of parastiches in the spiral patterns indicating  $L_p$ , the order of OAM of the pump beam.

101 spectra obtained for only one such mode combination –  $L_p = 7, \hat{x}$  and  $L_s = 8$  [green curves in Fig. 2(a)].  
102 Note that while their spectral shapes are similar to the conventional case where the pump is in  $\hat{\sigma}^\pm$   
103 polarization, power in the Raman band is dramatically suppressed by  $\sim 20$  dB for the *same* pump powers  
104 and mode sizes (intensity overlaps) [18]. Finally, the blue curves in Fig. 2(a) are Raman spectra for the  
105 Stokes mode in  $L_s = L_p - 1$ . Due to the perfect polarization overlap at every position along the fiber [Fig.  
106 1(e)], a strong Raman gain peak with strength similar to that of co-polarized Raman scattering (red curves)  
107 is obtained at the beat length matching wavelength  $\lambda_b$  where  $\Delta k = 0$ . Furthermore, the Raman spectrum  
108 is re-shaped and narrowed (yellow shaded region under blue curve) since  $\Delta k$  increases as Stokes  
109 wavelength deviates from  $\lambda_b$ . Additional sharp peaks evident on every spectral plot arise from the  
110 multitude of parametric FWM interactions that are also possible in these fibers [19] – as described in  
111 Supplement 1, these neither influence, nor change the conclusions evident from the Raman spectra. The  
112 modulated Raman peak wavelength  $\lambda_b$  shifts as pump mode changes since the  $\Delta k = 0$  condition is  
113 strongly dependent on the spectral dispersion of the modes, as well as, crucially, the topological charge  
114 that the pump mode carries. Hence, Fig. 2(a) illustrates the ability to tailor both the strength and  
115 wavelength of Raman emission by controlling the angular momentum content of light.

116 Figure 3(a) shows the integrated Raman power for the three functionally distinct mode  
117 combinations described in Fig. 2. The red curve represents the co-polarized Raman scattering process  
118 where both pump and Stokes light are in the  $\hat{\sigma}^-$  polarization, with each data point and error bar denoting  
119 the average and deviation of Raman strength in all Stokes modes for a given  $L_p$ . Despite the fact that the  
120 error bar for the  $L_p = 11$  case is large, due mainly to superimposed spectra from parasitic FWM (see  
121 Supplement 1), the flat trend with respect to  $L_p$  confirms conventional wisdom, that Raman strength does  
122 not depend on the phases of the participating waves (note that topological charges essentially manifest in  
123 the spatial phase of a mode). In contrast, when the pump light is an optically active state arising from SOI

124 interactions, all but one of the Stokes modes experience phase mismatches due to non-zero  $\Delta k$ , and  
 125 Raman power is suppressed by  $\sim 20$  dB, as illustrated with the green curve of Fig. 3(a) (again, large  
 126 measurement errors for  $L_p = 9, 12$  arise from parasitic FWM, but do not, otherwise, influence the  
 127 observed trend). For the Stokes mode corresponding to  $L_S = L_p - 1$ , we observe a systematic tunability  
 128 of Raman strength over 15 dB since the Raman spectra are now tailored by the  $\Delta k = 0$  condition [blue  
 129 curve in Fig. 3(a)]. The spectral position of peak Raman gain now depends not only on the conventional  
 130 Raman scattering strength of the material, but also its relation to the beat-length-matched wavelength  $\lambda_b$ .  
 131 Figure 3(b) shows this new degree of freedom – the ability to tune the Raman gain peak wavelength  $\lambda_b$ ,  
 132 simply by tuning the topological charge of the pump mode, by over 30 nm ( $\sim 8$  THz), which is greater than  
 133 half of the material's (Silica's) conventional Raman Stokes shift ( $\sim 13$  THz).

134 Further affirmation of this phase-matched behavior is evident from recording the bandwidth of the  
 135 modified Raman spectra [yellow shaded regions of Fig. 2(a)] as a function of fiber length. The spectra of  
 136 self-phase matched, conventional Raman scattering should display no inherent dependence on interaction  
 137 length, at least in the spontaneous scattering regime. In contrast, processes that have strict phase  
 138 matching requirements, such as second harmonic generation, have a response that is proportional to both  
 139 phase mismatch  $\Delta k$  and propagation distance  $z$ :

$$140 \quad I \propto \text{sinc}^2 \left( \frac{\Delta k \cdot z}{2} \right) \quad (4)$$

141 Since  $\Delta k$  maps to frequency, the bandwidth of a parametric process is inversely proportional to  $z$ .  
 142 Figure 3(c) plots the simulated  $\Delta k \cdot z/2$  values and Fig. 3(d) shows the corresponding experimentally  
 143 recorded Raman spectra of  $L_p = 15$ ;  $L_S = 14$ , for two different fiber lengths – 9.8m and 20m – shown in  
 144 blue and red curves, respectively. The green band in the simulations indicate the spectral limits of  $\Delta k \cdot z/2$   
 145 at which the nonlinear response is halved [per Eq. (4)]. Remarkably, not only do these intersection points

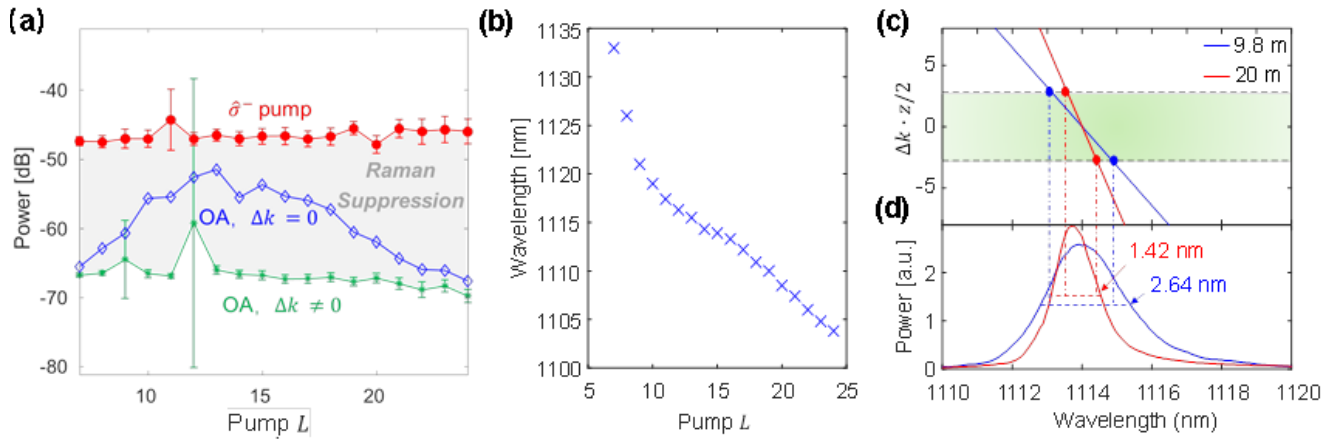


**Fig. 3.** (a) Integrated Raman power within 20 nm wavelength range for different pump-Stokes mode combinations, red: Raman power for  $\{\text{Stokes in } L_S, \hat{\sigma}^-; \text{Pump in } L_p, \hat{\sigma}^-\}$ ; green: Raman power for  $\{L_S \neq L_p - 1; L_p, \hat{x}\}$  combination, i.e.  $\Delta k \neq 0$ ; blue: Raman power for  $\{L_S = L_p - 1; L_p, \hat{x}\}$  combination, i.e.  $\Delta k = 0$ . Relatively larger error bars for some datapoints in red and green curves represent cases where a coincident, parasitic FWM peak existed, corrupting measurement of Raman power alone. (b) Peak wavelengths shift for Stokes mode in  $L_S = L_p - 1$  as a function of pump mode  $\{L_p, \hat{x}\}$ . (c) Simulated plot of phase mismatch multiplied by fiber length as a function of wavelength for  $\{L_S = 14; L_p = 15, \hat{x}\}$  mode combination. (d) Experimentally measured Stokes Raman spectral shape for  $\{L_S = 14; L_p = 15, \hat{x}\}$  mode combination in both 9.8 and 20-m-long ring-core fibers.

146 correspond well with the measured Raman spectra for the two lengths, the measured bandwidth ratio  
 147 (1.42 nm/2.64 nm) also closely corresponds to the fiber length ratio (9.8 m/20 m). This length dependence  
 148 of an otherwise self-momentum conserved scattering process illustrates the centrality of the role of phase  
 149 matching arising from SOI interactions.

150

151 **Discussion:**

152 The ability to modulate Raman scattering strength by  $\sim 20$  dB and to spectrally tune it by over  $\frac{1}{2}$  the  
 153 Raman gain bandwidth by controlling light's topological charge yields a design degree of freedom to  
 154 enhance, spectrally shape, or avoid Raman scattering, as applications as diverse as spectroscopy, lasers or  
 155 quantum sources may demand. The fact that the phase of light plays a role opens this important nonlinear  
 156 process to control via dispersion engineering – an established design tool for fibers and waveguides. Finally,

157 since the underlying effect arises from SOI of topologically complex light, systems other than waveguides,  
158 such as tightly focused light in bulk media, or OAM beams in chiral media, which would experience SOI or  
159 optical activity, may yield similarly anomalous Raman scattering dependencies, enabling control of Raman  
160 scattering in media other than waveguides too.

## 161 **References**

- [1] R. W. Boyd, *Nonlinear Optics* (Elsevier, ed. 4, 2020).
- [2] G. P. Agrawal, *Nonlinear Fiber Optics* (Elsevier, ed. 6, 2019).
- [3] L. D. Barron, M. P. Bogaard, A. D. Buckingham, "Raman scattering of circularly polarized light by optically active molecules," *J.Am.Chem.Soc.* **95**, 603-605 (1973).
- [4] F. M. Mitschke, L. F. Mollenauer, "Discovery of the soliton self-frequency shift," *Opt.Lett.* **11**, 659–661 (1986).
- [5] L. Rishøj, B. Tai, P. Kristensen, S. Ramachandran, "Soliton self-mode conversion: revisiting Raman scattering of ultrashort pulses," *Optica* **6**, 304-308 (2019).
- [6] A. Antikainen, L. Rishøj, B. Tai, S. Ramachandran, "Fate of a soliton in a high order spatial mode of a multimode fiber," *Phys.Rev.Lett.* **122**, 023901 (2019).
- [7] JX Cheng, X. S. Xie, "Vibrational spectroscopic imaging of living systems: An emerging platform for biology and medicine," *Science* **350**, aaa8870 (2015).
- [8] S. Laing, L. E. Jamieson, K. Faulds, D. Graham, "Surface-enhanced Raman spectroscopy for in vivo biosensing," *Nat.Rev.Chem.* **1**, 1-19 (2017).
- [9] M. D. Eisaman, J. Fan, A. Migdall, S. V. Polyakov, "Invited review article: Single-photon sources and

detectors," *Rev.Sci.Instrum.* **82**, 071101 (2011).

[10] C. Jauregui, J. Limpert, A. Tünnermann, "High-power fibre lasers," *Nat.Photonics* **7**, 861-867 (2013).

[11] J. W. Nicholson, J. M. Fini, A. M. DeSantolo, X. Liu, K. Feder, P. S. Westbrook, V. R. Supradeepa, E. Monberg, F. DiMarcello, R. Ortiz, C. Headley, D. J. DiGiovanni, "Scaling the effective area of higher-order-mode erbium-doped fiber amplifiers," *Opt.Express* **20**, 24575-24584 (2012).

[12] J. K. Sahu, S. Yoo, A. J. Boyland, A. S. Webb, M. Kalita, J. N. Maran, Y. Jeong, J. Nilsson, W. A. Clarkson, D. N. Payne, "Fiber design for high-power fiber lasers," *Fiber Lasers VI: Technology, Systems, and Applications.* **7195**, 71950I (2009).

[13] H. Takesue, K. Inoue, "1.5- $\mu\text{m}$  band quantum-correlated photon pair generation in dispersion-shifted fiber: suppression of noise photons by cooling fiber," *Opt. Express* **13**, 7832-7839 (2005).

[14] S. Ramachandran, P. Gregg, P. Kristensen, S. E. Golowich, "On the scalability of ring fiber designs for OAM multiplexing," *Opt.Express* **23**, 3721-3730 (2015).

[15] A. P. Greenberg, G. Prabhakar, S. Ramachandran, "High resolution spectral metrology leveraging topologically enhanced optical activity in fibers," *Nat.Comm.* **11**, 5257 (2020).

[16] G. Long, R. Sabatini, M. I. Saidaminov, G. Lakhwani, A. Rasmita, X. Liu, E.H. Sargent, W. Gao, "Chiral-perovskite optoelectronics," *Nat.Rev.Mater.* **5**, 423-439 (2020).

[17] K. Rottwitt, J. G. Koefoed, K. Ingerslev, P. Kristensen, "Inter-modal Raman amplification of OAM fiber modes," *APL.Photonics* **4**, 030802 (2019).

[18] X. Liu, A. Antikainen, Z. Ma, P. Kristensen, S. Ramachandran, "Suppression of Raman scattering by controlling the angular momentum content of fiber modes," in *CLEO*, FM2P.5. (2020).

[19] X. Liu, E. N. Christensen, K. Rottwitt, S. Ramachandran, "Nonlinear four-wave mixing with enhanced diversity and selectivity via spin and orbital angular momentum conservation," *APL photonics* **5**, 010802

(2020)

[20] M. E. V. Pedersen, P. Kristensen, L. Gruner-Nielsen, K. Rottwitt "Impact of the scalar approximation on the prediction of the group velocity dispersion," *J. Light. Technol.* **29**, 3129-3134 (2011).

[21] D. L. Vitullo, C. C. Leary, P. Gregg, R. A. Smith, D. V. Reddy, S. Ramachandran, M. G. Raymer, "Observation of interaction of spin and intrinsic orbital angular momentum of light," *Phys. Rev. Lett.* **118**, 083601(2017).

[22] S. D. Johnson, Z. Ma, M. J. Padgett, S. Ramachandran, "Measurement of the spin-orbit coupling interaction in ring-core optical fibers," *OSA Continuum* **2**, 2975-2982 (2019).

[23] F. Poletti, P. Horak, "Description of ultrashort pulse propagation in multimode optical fibers," *JOSA B* **25**, 1645-1654 (2008).

[24] R. H. Stolen, E. P. Ippen, A. R. Tynes, "Raman oscillation in glass optical waveguide," *Appl. Phys. Lett.* **20**, 62-64 (1972).

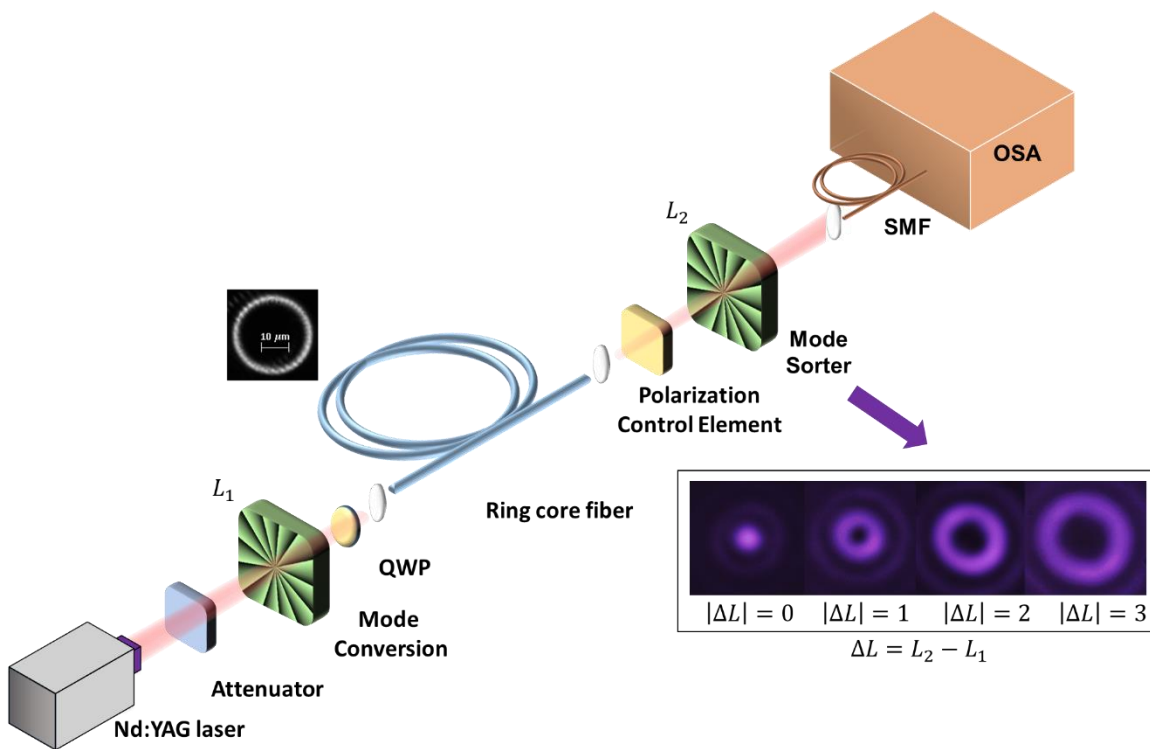
162 **Supplementary Materials:** Systematic control of Raman scattering with topologically  
163 induced chirality of light

164 **Materials and methods**

165 **Detailed experiment setup**

166 Figure S1 illustrates the experimental setup: We use a homemade laser source that comprises a  
167 Nd:YAG seed laser and 1.5-m-long Yb-doped fiber amplifier that produces 0.65 ns, up to 120 kW peak  
168 power, pulses at the repetition rate of 19.5 kHz. The attenuator consists of a half wave plate and  
169 polarization beam splitter, which serves the purpose of controlling power and ensuring output light in  $\hat{x}$   
170 polarization, which is the preferred polarization for the spatial light modulator (SLM). The input Gaussian  
171 beam is then converted into the desired OAM state with topological charge  $L$  using a SLM encoded with  
172 spiral phase, and the spin angular momentum (SAM) of light is controlled with a quarter wave plate (QWP).  
173 In our experiment, we specifically compare  $\hat{\sigma}^-$  and  $\hat{x}$ -polarized OAM states. The free space OAM beam is  
174 then coupled into the specially designed ring-core fiber that supports stable propagation of multiple OAM  
175 beams, a detailed analysis of the fiber and modes properties is presented in §1. At the output, the  
176 polarization control element varies for the two different pump polarization cases: (1) for the experiments  
177 in which the pump is in the  $\hat{x}$  polarization, it only comprises a linear polarizer (LP) whose axis is sequentially  
178 set to horizontal and vertical positions for interrogating the output nonlinear spectra in  $\hat{x}$  and  $\hat{y}$   
179 polarizations, respectively; (2) for the cases where the pump is in the  $\hat{\sigma}^-$  polarization, we add a QWP, and  
180 the combination of the QWP and LP acts as a circular polarizer, which allows us to measure light in  $\hat{\sigma}^\pm$   
181 polarizations separately. We use a second SLM and a single mode pick up fiber (part number SM980, called  
182 just SMF, henceforth) to modally sort the spectrum by its topological charge. The basic principle of the  
183 mode sorting function can be understood as follows: the OAM beam from the output of the fiber, with  
184 topological charge  $L_1$ , is incident on the mode sorter SLM which has another spiral phase pattern of OAM  
185 value  $L_2$ . The resultant beam, upon reflection from this SLM, has an OAM value of  $\Delta L = L_1 - L_2$ . For all

186 input beams resulting in non-zero  $\Delta L$ , light remains in a donut-shaped OAM mode in free space (see inset  
 187 of Fig. S1) and cannot be coupled into the single mode fiber. In contrast, for  $L_1 = L_2$ , the OAM gets  
 188 cancelled and the output is converted to a Bessel beam with *zero* OAM in free space, which can now couple  
 189 into the SMF. Hence, the mode sorter SLM and SMF combination can selectively measure spectra only in  
 190  $L_2$ . Furthermore, by sweeping  $L_2$  and obtaining the spectra from each orthogonal polarization, we are able  
 191 to measure the total output spectra in each individual mode.



192

193 **Fig. S1.** Detailed experiment setup, the attenuator is comprised of a half wave plate and polarization beam  
 194 splitter, mode conversion and mode sorter are two identical SLMs with different spiral phase patterns, the  
 195 polarization control element varies from a single LP and a combination of QWP and LP depending on the  
 196 pump polarizations, details discussed in §1. The inset picture shows the free-space reconverted beam  
 197 shape for different OAM values of two SLMs. SMF: single mode fiber, OSA: optical spectrum analyzer.

198

199 **Mode sorter setup characterization**

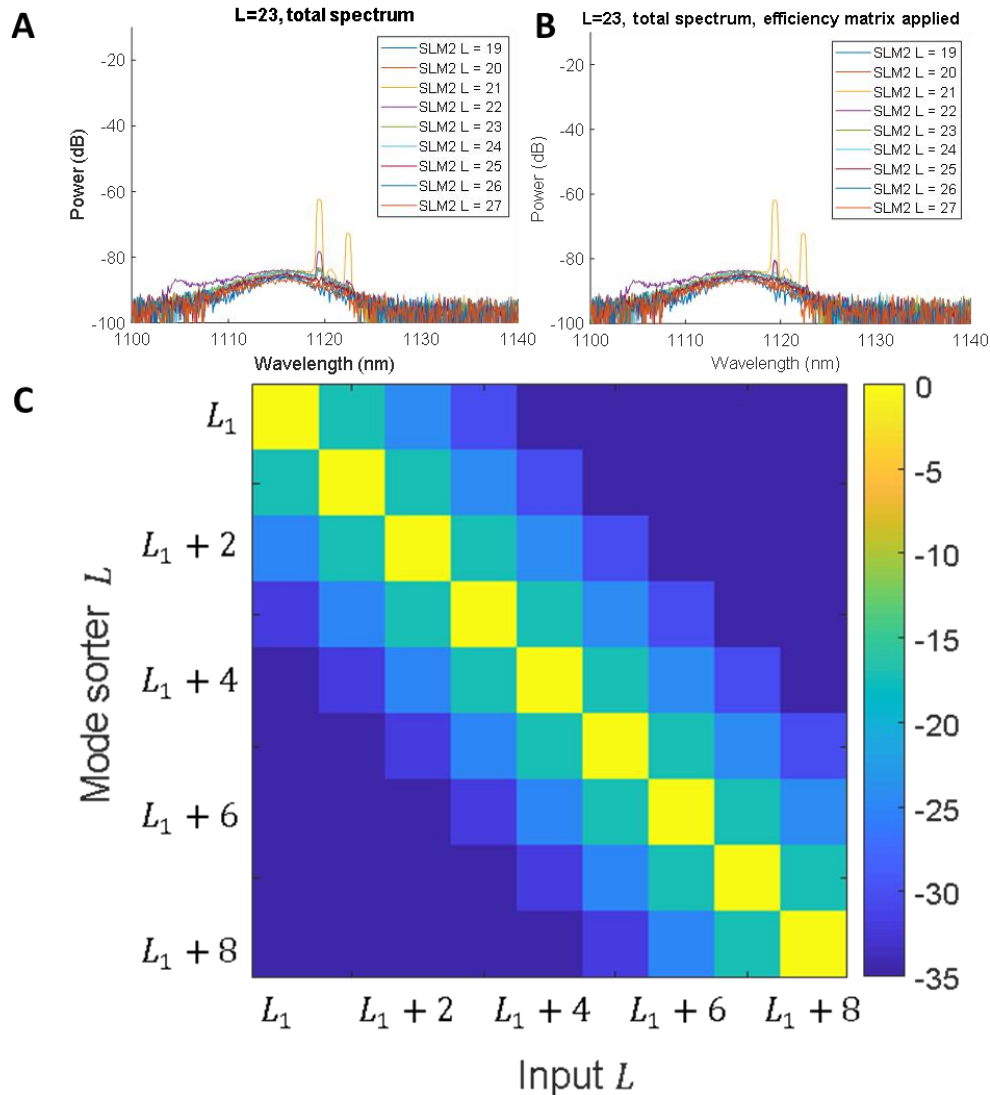
200 Since the extinction ratio of the mode sorter is finite, the spectral contribution of one mode may  
 201 appear in other modes as well, which is especially problematic for weeding out contributions from

202 parasitic FWM processes, which are typically intense. Figure. S2A shows the mode-sorted nonlinear  
 203 spectra for the participating modes when pumping in an  $L = 23$ , OA state. The sharp peak showing up at  
 204 1119.52 nm is expected to be due to FWM, and should reside in the  $L = 21$  mode according to simulated  
 205 phase matching conditions (discussed in more detail in §2). The experiment confirms this prediction – see  
 206 yellow curve in Fig. S2A. However, due to the limited extinction ratio of the mode sorter, we also get the  
 207 projection of this spectrum in the other modes, necessitating the need for calibration of our mode-sorter,  
 208 based on the a priori knowledge that the FWM spectrum should have resided only in a specific mode of  
 209 given  $L$ . We set up the relationship between the actual mode power  $P$  and measured power  $P'$  at the  
 210 output of SMF through the efficiency matrix in Eq. S1, where each element  $\eta_{m,n}$  in the matrix stands for  
 211 the coupling efficiency for input light in  $L_m$  when SLM spiral phase pattern is set to be  $L_n$ ,

$$212 \begin{bmatrix} P'_i \\ P'_{i+1} \\ \vdots \\ P'_j \end{bmatrix} = \begin{bmatrix} \eta_{i,i} & \eta_{i+1,i} & \cdots & \eta_{j,i} \\ \eta_{i,i+1} & \eta_{i+1,i+1} & \cdots & \eta_{j,i+1} \\ \vdots & \vdots & \ddots & \vdots \\ \eta_{i,j} & \eta_{i+1,j} & \cdots & \eta_{j,j} \end{bmatrix} \cdot \begin{bmatrix} P_i \\ P_{i+1} \\ \vdots \\ P_j \end{bmatrix} \quad (S1)$$

213 To characterize all the elements in the efficiency matrix, a pure OAM state input is required.  
 214 Nonlinearly generated OAM modes due to FWM are excellent candidates in this regard since phase  
 215 matching and OAM conservation conditions ensure single mode emission at the phase-matched  
 216 wavelength [19]. Each column of the matrix is acquired by measuring coupling efficiency for input light,  
 217 expected to be purely in  $L_m$ , and sweeping SLM phase pattern  $L_n$  from  $L_m - 4$  to  $L_m + 4$ . Probing spectra  
 218 in modes  $|L_m - L_n| > 4$  is not necessary since the coupling efficiency is negligibly small ( $< -40$  dB). By  
 219 sweeping  $L_m$  and repeating the measurements, we can construct the whole efficiency matrix. We perform  
 220 an independent calibration matrix measurement by sweeping  $L_m$  from 5 to 28, since the power in  
 221 neighboring modes is very sensitive to change of  $L_m$  for extinction ratios greater than -15 dB. We take the  
 222 average for all the extinction ratio measurements and create an average efficiency matrix (Fig. S2C).

223 Hence, we conclude that the extinction ratio is -17 dB for  $\Delta L = \pm 1$ , -24 dB for  $\Delta L = \pm 2$ , -30 dB for  $\Delta L =$   
 224  $\pm 3$ . We then apply the efficiency matrix to the measurement by Eq. S1 to further improve the  
 225 measurement accuracy, as is shown in Fig. S2B. As is evident, peaks at 1192.52 nm in the unexpected  
 226 modes are substantially suppressed compared to those in Fig. S2A, allowing for precise measurements of  
 227 the modal content of output spectra.



228

229 **Fig. S2. (A)** Mode sorted spectrum for pump in  $L = 23$ , OA state without applying the efficiency matrix,  
 230 sharp peaks at  $\sim 1120$  nm correspond to FWM Stokes peak in  $L = 22$ . **(B)** Mode sorted spectrum for pump  
 231 in  $L = 23$ , OA state after applying the efficiency matrix per Eq. S1. **(C)** Calibrated efficiency matrix, each  
 232 column corresponds to the coupling efficiency when sweeping the mode sorter OAM value, the noise floor  
 233 of the system is set to be -35 dB, which is restricted by the detector noise floor.

## 234 Supplementary Text

### 235 1) Fiber design

#### 236 1a) Fiber profile and effective index of guided modes

237 The refractive index profile of the ring-core fiber used in our experiments is measured with a  
238 commercial interferometer-based fiber index profiler (Interfiber Analysis: IFA-100), and the refractive  
239 index  $\Delta n(r)$  relative to Silica index is shown in Fig. S3A. The OAM modes are guided in the ring structure  
240 region whose inner diameter and thickness are  $21 \mu\text{m}$  and  $5 \mu\text{m}$ , respectively. The large refractive index  
241 step of 0.038 evident in Fig. S3A enables a large mode volume as well as significant separation of the  
242 effective index  $n_{eff}$  (related to the propagation constant  $\beta$  of a mode by  $n_{eff} = \beta\lambda/2\pi$ ), among modes.  
243 This separation  $\Delta n_{eff}$ , especially between modes of same  $|L|$  but different combinations of OAM and SAM  
244 signs (called the spin-orbit aligned (SOa) modes when  $L$  and  $\hat{\sigma}$  have the same sign and spin-orbit anti-  
245 aligned (SOaa) modes when they have opposite signs) is a key feature ensuring stability of not only each  
246 individual OAM mode<sup>16</sup>. The mode simulation is performed by solving the full-vectorial wave equation  
247 with a finite-difference scheme [21] and the wavelength dependent effective indices are presented in Fig.  
248 3B. Each color represents modes with different topological charges and is comprised of two curves for  
249 SOa-SOaa pairs of same  $L$ . As is shown in the inset figure in Fig. 3B, the solid purple line corresponds to  
250  $L = 19, SOaa$  state and the dashed purple line corresponds to  $L = 19, SOa$  state, the separation between  
251 these two modes is usually on the order of  $10^{-5}$ , which is orders of magnitude smaller than  $\Delta n_{eff}$   
252 between different  $L$ 's ( $\sim 10^{-3}$  as indicated by the blue arrows), hence it looks like they overlap with each  
253 other in Fig. 3B.  $\Delta n_{eff}$  between these pairs of non-degenerate modes arises from spin-orbit interactions  
254 and usually increases monotonically with  $L$  (discussed in more detail in §1b). From our experience, stable  
255 guidance of each mode from these pairs is ensured for  $\Delta n_{eff} \sim 5 \times 10^{-5}$ , especially for the meter-long  
256 fibers used in our experiments. This would suggest that the lowest mode order stably guided in this fiber

257 is  $L = 21$ . However, experimentally, we found that even lower order modes are also guided stably – an  
 258 anomalous result which we discuss in greater details in §1b. The highest (cutoff) mode is determined by  
 259 the relative position of the  $n_{eff}$  curve to the refractive index of Silica at that wavelength (calculated from  
 260 Silica’s Sellmeier equation and plotted as the black dashed curve in Fig, 3B). Conventionally, any  $n_{eff}$  curve  
 261 that is below the Silica index curve is considered to be beyond cutoff, hence in this case,  $L = 25$  is  
 262 expected to be the highest mode order supported by the fiber at the pump wavelength at 1064 nm.

263

### 264 1b) Spin-orbit interaction (SOI)

265 A spin-orbit interaction in fibers arises from the anisotropy of the fiber’s refractive index distribution.  
 266 It serves to split the  $n_{eff}$  for two circularly polarized modes of same  $L$  by [22]:

$$267 \quad \Delta n_{eff} = \frac{\lambda^2 L}{4\pi^2 a^2 n_{co}^2} \int_0^\infty |E(r)|^2 \frac{\partial \Delta n(r)}{\partial r} dr \quad (S2)$$

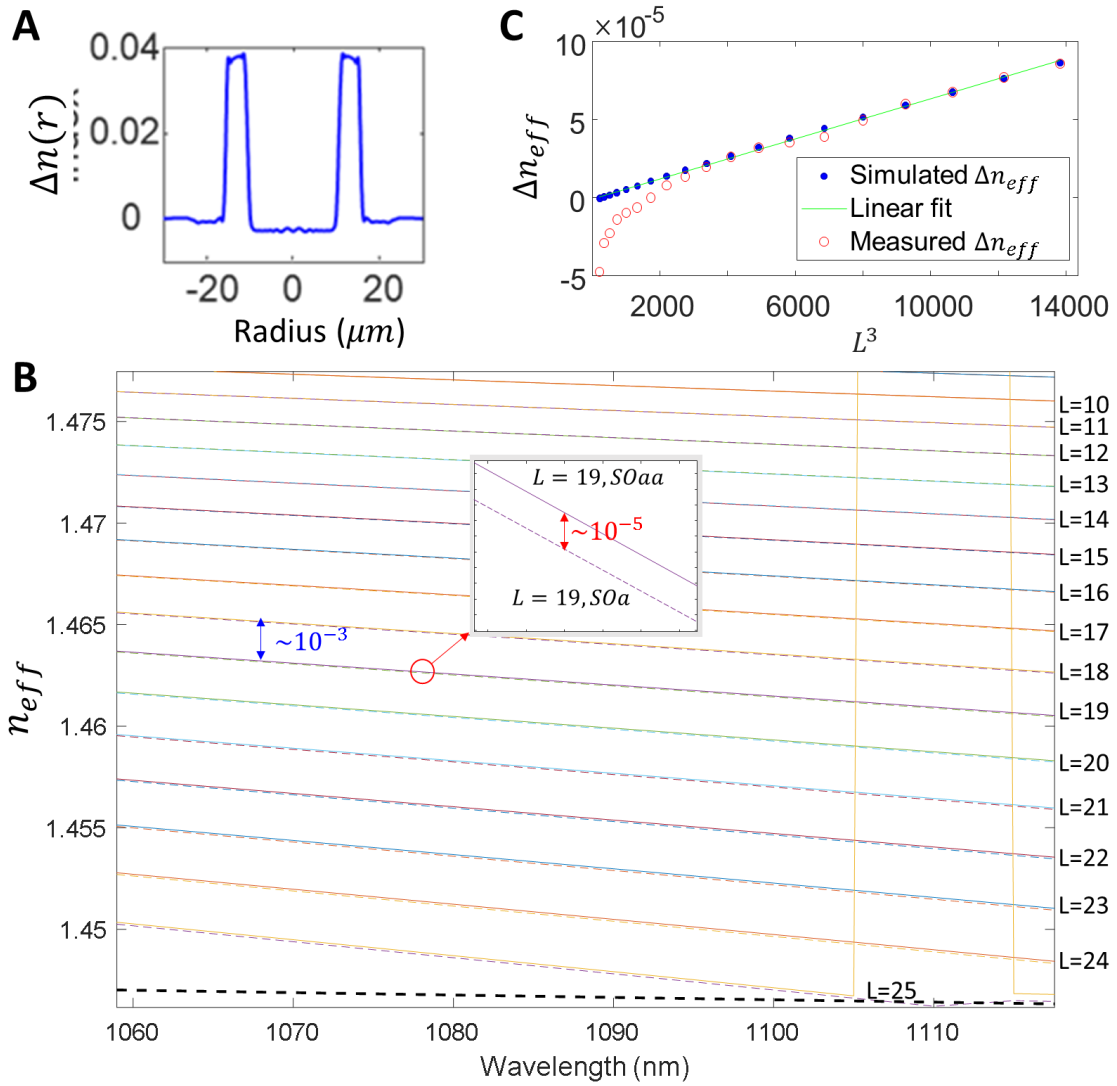
268 where  $r$  is the radial coordinate,  $E(r)$  is the normalized electric field for the unperturbed mode,  $a$  is the size  
 269 of the fiber core,  $\lambda$  is the free-space wavelength, and  $n_{co}$  is the maximum refractive index. Note the  
 270 similarity of this equation with SOI in atomic systems, where eigenstate splitting increases with  $L$ . The ring-  
 271 core design of Fig. S3A is among a class of fiber designs that exacerbates this splitting, which, in turn,  
 272 ensures that each of the modes propagates in these fibers stably<sup>16</sup>.

273 The exact dependence of  $\Delta n_{eff}$  on  $L$  is influenced by how the field  $E(r)$  varies with  $L$  [23]. For the fiber  
 274 shown in Fig. S3A,  $\Delta n_{eff}$  scales as  $L^3$ , as evident from Fig. S3C, which plots the simulated  $\Delta n_{eff}$  versus  $L^3$   
 275 in blue as well as its excellent match with a fit of a function  $y = constant * L^3$  (shown in green, linear  
 276 regression  $R^2$  coefficient 0.999). To experimentally verify this relationship, we measure  $\Delta n_{eff}$  values for  
 277 each  $L$  based on the linear polarization rotation angle  $\theta_{OA}$  of their corresponding OA state, which is  
 278 defined as<sup>6</sup>:

279  
280  
281  
282  
283  
284  
285  
286  
287  
288  
289  
290  
291  
292  
293  
294  
295  
296  
297  
298  
299  
300

$$\theta_{OA} = \frac{\pi \Delta n_{eff}}{\lambda} d \quad (S3)$$

where  $d$  represents the propagation distance and can be accurately measured via cutback. Hence, we can calculate  $\Delta n_{eff}$  by launching an  $\hat{x}$ -polarized (OA) light into the fiber and measuring  $\theta_{OA}$  at the output with an LP. To avoid the issue of uncertainties arising from unwrapping the measured phase angles, our cutback length  $d$ , were set to be less than 1 cm, hence ensuring  $\theta_{OA} \in [0, \pi]$  for all the  $L$ 's. The measured  $\Delta n_{eff}$  vs.  $L^3$  is plotted as the red circles in Fig. 3C. While the measurements agree well the simulation results for modes of higher  $L$ , the mismatch gets larger as  $L$  decreases. The origin of this discrepancy is likely from an incorrect measurement of  $\Delta n(r)$  on two accounts. Firstly, no refractive index profiler would have arbitrary spatial resolution, and as Eq. S2 shows,  $\Delta n_{eff}$  is sensitive to the *gradient* of this measurement. Secondly, and perhaps more importantly, we believe that the anomalously large (but opposite in sign)  $\Delta n_{eff}$  one experimentally observes for lower  $L$  modes arises from the fact that low  $L$  modes have larger field amplitudes closer to the inner ring-core boundary, and large stresses and strains due to the large  $\Delta n(r)$  at this boundary result in inherent radial or azimuthal birefringence. That is,  $\Delta n(r)$  is now a vector quantity and the spin-orbit splitting cannot be simply represented by Eq. S2. This is speculation (by elimination of other possible causes), of course, and confirming the origins of the large  $\Delta n_{eff}$  for low  $L$  modes will require more in-depth measurement of the permittivity tensor [and not just the scalar  $\Delta n(r)$ ] of the fiber profile.



301

302 **Fig. S3. (A)** Refractive index  $\Delta n(r)$  of the ring-core fiber used in the experiment, the index profile is relative  
303 to the index of Silica, which is the material that forms the cladding of the fiber. **(B)** Effective index ( $n_{eff}$ )  
304 for all the OAM modes as a function of wavelength, the black dashed line corresponds to the refractive  
305 index of Silica calculated by the Sellmier equation. The inset figure shows the zoomed-in  $n_{eff}$  in the red  
306 circle region.  $n_{eff}$  curves for each  $L$  consist of a solid and dashed line, representing, respectively, the SOaa  
307 and SOa modes. **(C)** Spin-orbit interaction (SOI) induced splitting  $\Delta n_{eff}$  of SOa-SOaa mode-pairs for the  
308 variety of OAM ( $|L|$ ) orders probed in our experiments. Blue: Simulated  $\Delta n_{eff}$  as a function of  $L^3$ , green:  
309 linear fit of  $\Delta n_{eff}$  vs.  $L^3$ , red: measured  $\Delta n_{eff}$  as a function of  $L^3$ .

310

311

312

313

314 2) Parasitic Four Wave Mixing process

315 As mentioned in the context of Fig. 2A, the additional sharp spectral features shown on top of the blue  
 316 curves result from FWM among different OAM modes. They are unavoidably present, given the diversity  
 317 of phase matching conditions arising from the plethora of available modes. Their emission wavelengths  
 318 are determined by the conventional phase matching condition [20]:

$$319 \quad \Delta\beta = \frac{n_{eff}^p(\lambda_p)}{\lambda_p} + \frac{n_{eff}^q(\lambda_q)}{\lambda_q} - \frac{n_{eff}^s(\lambda_s)}{\lambda_s} - \frac{n_{eff}^{as}(\lambda_{as})}{\lambda_{as}} = 0 \quad (S4)$$

320 where  $p, q, s$  and  $as$  represent the first and second pumps, Stokes and anti-Stokes beams, respectively.

321 This nonlinear process must also conserve angular momentum, and so:

$$324 \quad -L_p - L_q + L_s + L_{as} = 0 \quad (S5)$$

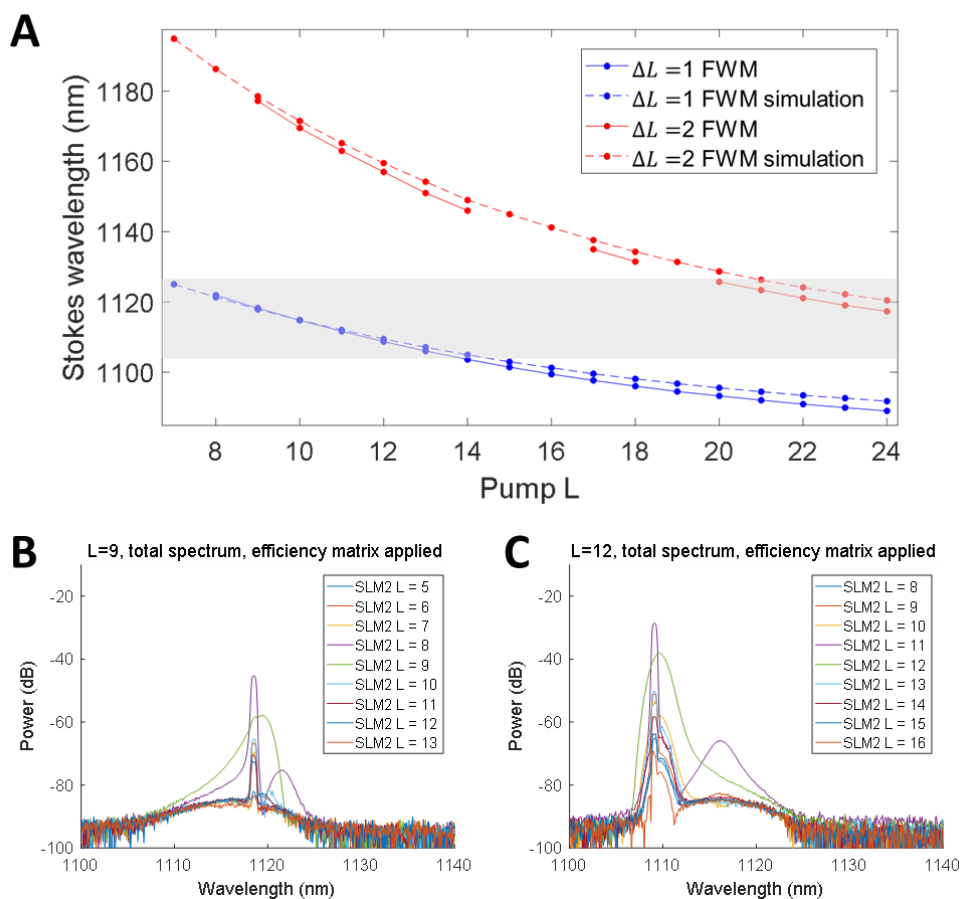
322 Hence strong emissions happen only when both the residual topological charge is equal to 0 and the phase  
 323 matching condition is fulfilled. In our experiment, we usually observe two FWM processes:

$$325 \quad L_s = L_p + 1 \leftarrow L_p + L_p \rightarrow L_{as} = L_p - 1 \quad (S6)$$

$$326 \quad L_s = L_p + 2 \leftarrow L_p + L_p \rightarrow L_{as} = L_p - 2 \quad (S7)$$

327 here we refer to Eq. S6 and S7 as  $\Delta L = 1$  and  $\Delta L = 2$  FWM processes, where the pumps are degenerate  
 328 in topological charge  $L_p = L_q$ , anti-Stokes light is one or two mode orders lower than that of the pump,  
 329 and hence according to Eq. S4, Stokes light is in one or two mode orders higher. Combining Eqs. S4-7, we  
 330 can simulate the Stokes light wavelengths and compare with experiment – as is shown in Fig. S4A, we find  
 331 excellent agreement, with wavelength deviations to be less than 3 nm for any of the FWM processes.  
 332 When the FWM Stokes wavelength falls into the grey band (see Fig. 2A) where material Raman gain  $g_R(\Omega)$   
 333 is substantial, the spectra due to Stokes Raman scattering and FWM become hard to distinguish, with the  
 334 FWM peaks showing up as sharp features on top of the broad Raman peak. These extraneous peaks can  
 335 be easily excluded when calculating integrated Raman power in most cases, since they are relatively

336 narrowband compared to the (Raman) spectra of interest to us. However, in two special cases, specifically,  
 337 when the pump is in the  $L = 9$ ; OA or  $L = 12$ ; OA modes, we also observed broadband FWM emissions  
 338 on top of Raman (see Fig. S4B and S4C), which correspond to degenerate  $L$  FWM process where all the  
 339 interacting photons are in the same  $L$ . Since the bandwidth is almost similar to the Raman gain peak, large  
 340 error bars result in integrated Raman power at those data points in Fig. 3A. We had argued that the large  
 341 error bars may be ignored because the rest of the data points do indeed follow the trend we observe –  
 342 below, in §3b, we offer additional assurance for the validity of this assumption.



343

344 **Fig. S4. (A)** Stokes wavelength for two different types of four wave mixing process, red curves correspond  
 345 to  $\Delta L = 1$  FWM process where the Stokes and anti-Stokes mode are 1 mode order away from the pump,  
 346 and blue curves correspond to  $\Delta L = 2$  FWM process. Dashed lines are simulation results and solid lines  
 347 are experimentally measured. **(B)** Mode sorted spectra when pumping in  $L = 9$ , OA state, a broad band  
 348 FWM peak shows up at  $\sim 1120$  nm in the same mode as the pump  $L = 9$ . **(C)** Mode sorted spectra when  
 349 pumping in  $L = 12$ , OA state, similarly, a broad band FWM peak shows up at  $\sim 1110$  nm in the same mode  
 350 as the pump  $L = 12$ .

351 3) Multimode generalized nonlinear Schrödinger equation simulation

352 3a) Phase matching behavior of topological charge mediated Raman scattering process

353 In order to verify the phase dependence of the optical activity mediated Raman process, we perform  
 354 simulations by numerically solving the multimode generalized nonlinear Schrödinger equation<sup>24</sup>, which  
 355 can be written in the following form: (Shock term ignored for quasi-CW pulses)

$$\begin{aligned}
 356 \quad \frac{\partial A_p(z, t)}{\partial z} = & i(\beta_0^{(p)} - \beta_0) A_p(z, t) - (\beta_1^{(p)} - \beta_1) \frac{\partial A_p(z, t)}{\partial t} + i \sum_{n \geq 2} \frac{\beta_n^{(p)}}{n!} \left( i \frac{\partial}{\partial t} \right)^n A_p(z, t) \\
 357 \quad & + \frac{in_2\omega_0}{c} \sum_{l,m,n} \left\{ Q_{plmn}^{(1)}(\omega_0) 2A_l(z, t) \int d\tau R(\tau) A_m(z, t - \tau) A_n^*(z, t - \tau) \right. \\
 358 \quad & \left. + Q_{plmn}^{(2)}(\omega_0) A_l^*(z, t) \int d\tau R(\tau) A_m(z, t - \tau) A_n(z, t - \tau) e^{2i\omega_0\tau} \right\} \quad (S8)
 \end{aligned}$$

359 The overlap integrals can be written in the following form:

$$360 \quad Q_{plmn}^{(1)} = \frac{\varepsilon_0^2 n_0^2 c^2}{12} \int dx dy [F_p^*(\omega) \cdot F_l(\omega)] [F_m(\omega) \cdot F_n^*(\omega)] \quad (S9)$$

$$361 \quad Q_{plmn}^{(2)} = \frac{\varepsilon_0^2 n_0^2 c^2}{12} \int dx dy [F_p^*(\omega) \cdot F_l^*(\omega)] [F_m(\omega) \cdot F_n(\omega)] \quad (S10)$$

362 where  $F$  represents the normalized radial distribution of the mode electric field,  $R(\tau)$  stands for the  
 363 nonlinear response function, and can be written as:

$$364 \quad R(\tau) = (1 - f_R) \delta(t) + \frac{3}{2} f_R h(t) \quad (S11)$$

365 where  $f_R = 0.18$  is the fractional contribution of the Raman response to the total nonlinearity and  $h(t)$  is  
 366 the delayed Raman response function, modeled after the experimental Raman response function of silica  
 367 [24], and the delta function corresponds to Kerr effect. We first involve only 6 OAM modes with 3 different  
 368 topological charge values 14, 15, and 16 of both circular polarizations  $\hat{\sigma}^\pm$ . The input power and fiber length  
 369 are the same as in the experiments, i.e., 1.7 kW and 9.8 m. We assume a quasi-CW pulse, and quantum  
 370 shot noise is included as one photon with random phase per longitudinal mode (frequency bin) per OAM

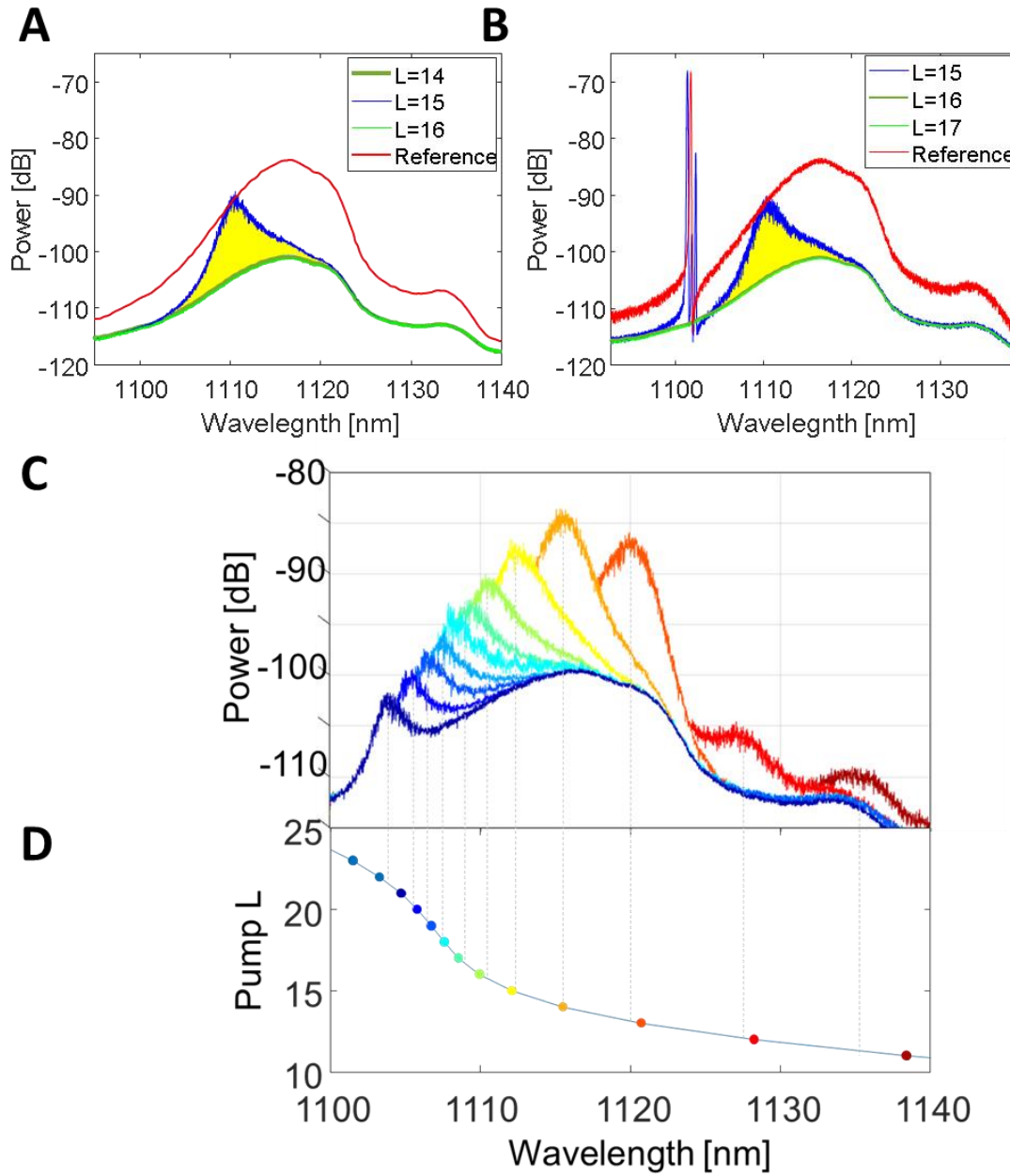
371 mode. Each spectrum shown is an average of 50 simulations with different random number generator  
372 seeds.

373 We start our simulation by pumping in only the  $L = 16, \hat{\sigma}^+$  mode. Note that for this specific mode  
374 combination, FWM among modes with different topological charges is prohibited because the pump mode  
375 has the highest  $L$ , and so scattering into  $L = 14$  or  $15$  would require a higher-order mode to be present  
376 according to the OAM conservation rule (Eq. S5). These higher-order modes have intentionally been  
377 omitted from the simulations for the purpose of studying the Raman effect without the presence of FWM.  
378 The comparison where FWM is included is discussed in §3b. The resultant spectra look very similar for all  
379 the  $L$ 's in the same polarization as that of the pump ( $\hat{\sigma}^+$ ), and we just select one mode (Stokes in  $L = 15$ )  
380 and show as the red curve in Fig. S5A, which represents the conventional co-polarized Raman gain  
381 spectrum. We then switch the pump to an OA state of the same  $L = 16$  while holding total power  
382 constant. As is evident from the dark and light green curves in Fig. S5A, Stokes light in  $L = 14$  and  $L = 16$   
383 are highly suppressed because they cannot fulfill the beat length matching condition across the Raman  
384 gain band, as illustrated in Fig. 1D. In contrast, for Stokes light in  $L = 15$ , we observe a narrow modulated  
385 Raman spectral shape that peaks at  $\sim 1110$  nm, which is determined by the beat length matching condition,  
386 as is also shown experimentally in Fig. 2A. To further support the idea of controlling Raman spectral shape  
387 by dispersion engineering, we keep  $P \cdot \eta$  constant and sweep pump  $L$  to acquire the Raman spectra in the  
388 beat-length-matched mode, as shown in Fig. S5C. The corresponding beat length matching wavelength  $\lambda_b$   
389 is plotted in Fig. S5D. The good match between simulated  $\lambda_b$  and the modulated Raman gain peak  
390 (indicated by the black dashed vertical lines) and analogous behavior shown in the experiments depicted  
391 in Fig. 2 supports our primary claim – that this topological effect is a manifestation of a heretofore  
392 unobserved phase matching behavior for Raman scattering.

393

395 3b) Four-wave-mixing effect on Raman scattering process

396 To probe whether the parasitic FWM peaks in our experiments affect, or otherwise modify, the phase-  
397 matched Raman scattering process, we simulate the behavior by intentionally turning on or off FWM.  
398 Above (§3a), we simulated the behavior by effectively turning off FWM. Now, we turn the effect on by  
399 replacing the  $L = 14$  mode with the  $L = 17$  mode in the ensemble of participating modes included in our  
400 simulation. The new choice of interacting modes are now  $L = 15, 16$  and  $17$ . For pump in  $L = 16$ ,  $\Delta L =$   
401  $1$  FWM (Eq. S6) processes are now allowed as both  $L = 15$  and  $17$  are included in the simulation. As  
402 evident from Fig. S5B, when pumping in a single mode in  $L = 16$ ,  $\hat{\sigma}^+$ , we obtain a similar conventional  
403 Raman scattering with FWM Stokes peak showing up at  $1100$  nm in  $L = 15$  (red curve). Changing the pump  
404 to the  $L = 16$ ,  $OA$  state yields suppression of Raman in the  $L = 16$  and  $17$   $OA$  modes as before (light and  
405 dark green curves in Fig. S5B). Finally, Stokes light in the  $L = 15$  mode yields a similarly modulated Raman  
406 spectrum as that shown in Fig. S5A, with the additional presence of FWM peaks in its spectral proximity.  
407 This proves that the large error bars for selected data points of Fig. 3A arising from FWM do not otherwise  
408 affect our central conclusions, since the influence of FWM is clearly distinct and separable from that of the  
409 Raman scattering process we have aimed to study.



410

411

412

413

414

415

416

**Fig. S5. (A)** Simulated spectra based on the multi-mode nonlinear Schrödinger equation, with FWM intentionally excluded by choice of modes. Red curve corresponds to pump in  $L = 16, \hat{\sigma}^+$ , Stokes in  $L = 15$ , dark and light green curves correspond to pump in  $L = 16$ , OA, Stokes in  $L = 14$  and  $16$ , blue curve corresponds to  $L = 16$ , OA, Stokes in  $L = 15$ , the yellow shaded regime indicates the tailored Raman spectral shape. **(B)** Comparison with the case where FWM is included, red curve corresponds to pump in  $L = 16, \hat{\sigma}^+$ , Stokes in  $L = 15$ , dark and light green curves correspond to pump in  $L = 16$ , OA, Stokes in

417  $L = 16$  and 17, blue curve corresponds to  $L = 16$ , OA, Stokes in  $L = 15$ . **(C)** Raman spectra in the beat  
418 length matching mode for pump in different  $L$ 's. **(D)** Simulated beat length matching wavelength as a  
419 function of pump  $L$ , black dashed line indicates good agreement with the modulated Raman gain peak  
420 wavelengths.